Icarus 273 (2016) 346–355

Contents lists available at ScienceDirect

Icarus

journal homepage: www.elsevier.com/locate/icarus

A new lunar digital elevation model from the Lunar Orbiter Laser Altimeter and SELENE Terrain Camera

M.K. Barker[a,*], E. Mazarico[b], G.A. Neumann[b], M.T. Zuber[c], J. Haruyama[d], D.E. Smith[c]

[a] Sigma Space Corporation, 4600 Forbes Blvd., Lanham, MD 20706, United States
[b] Goddard Space Flight Center, 8800 Greenbelt Rd., Greenbelt, MD 20771, United States
[c] Dept. of Earth, Atmospheric and Planetary Sciences, MIT, 77 Massachusetts Ave. Cambridge, MA 02139, United States
[d] Inst. of Space and Astronautical Sci., Japan Aerospace Exploration Agency, Japan

ARTICLE INFO

Article history:
Received 5 March 2015
Revised 5 June 2015
Accepted 12 July 2015
Available online 8 August 2015

Keywords:
Moon
Moon, interior
Moon, surface

ABSTRACT

We present an improved lunar digital elevation model (DEM) covering latitudes within ±60°, at a horizontal resolution of 512 pixels per degree (~60 m at the equator) and a typical vertical accuracy ~3 to 4 m. This DEM is constructed from ~ 4.5×10^9 geodetically-accurate topographic heights from the Lunar Orbiter Laser Altimeter (LOLA) onboard the Lunar Reconnaissance Orbiter, to which we co-registered 43,200 stereo-derived DEMs (each $1° \times 1°$) from the SELENE Terrain Camera (TC) (~10^{10} pixels total). After co-registration, approximately 90% of the TC DEMs show root-mean-square vertical residuals with the LOLA data of <5 m compared to ~ 50% prior to co-registration. We use the co-registered TC data to estimate and correct orbital and pointing geolocation errors from the LOLA altimetric profiles (typically amounting to <10 m horizontally and <1 m vertically). By combining both co-registered datasets, we obtain a near-global DEM with high geodetic accuracy, and without the need for surface interpolation. We evaluate the resulting LOLA + TC merged DEM (designated as "SLDEM2015") with particular attention to quantifying seams and crossover errors.

1. Introduction

The lunar surface records clues to the history of its formation, internal structure, composition, volcanism, and bombardment. Topographic maps play a crucial role in deciphering these. For example, topographic information is useful in the identification and characterization of craters and basins, important data for unraveling the impact history, thermal evolution, and stratigraphy of the Moon, as well as the impact cratering process (Pike, 1976; Melosh, 1989; Head et al., 2010; Baker et al., 2012; Fassett et al., 2012). In addition, topographic maps are necessary to account for gravity anomalies due to surficial density contrasts, and to assess the anomalies due to subsurface density variations (Neumann et al., 1996). The resulting Bouguer anomaly maps are crucial in understanding characteristics of the interior structure of the Moon, such as its crustal thickness (Wieczorek et al., 2013). Topographic maps are also useful in exploration and mission design studies to analyze potential landing sites and robotic traverses (Johnson et al., 2010; Potts et al., 2015).

Our knowledge of lunar topography has greatly improved over the last two decades with a combination of laser altimetry and imagery collected from orbiting spacecraft. Over the course of two months in 1994, the Clementine laser altimeter collected ~ 123,000 ground returns covering 79°S to 82°N with an along-track sampling of 20 km up to several hundred km, a cross-track spacing of ~ 60 km at the equator, and an absolute vertical accuracy of ~ 100 m (Smith et al., 1997). These data were filtered and assembled into a spherical harmonic model complete to degree and order 72 with a $0.25° \times 0.25°$ spatial grid (Smith et al., 1997), allowing estimates of the lunar figure, such as the mean radius and center-of-mass/center-of-figure offset.

Later, Archinal et al. (2006) released the Unified Lunar Control Network 2005 (ULCN2005), a photogrammetric network of 272,931 points based on 43,866 Clementine images and a previous network derived from Earth- and space-based images. By solving for the radii of the control points, the ULCN2005 avoided the kilometer-scale horizontal distortions present in previous networks. A by-product of the network was a global topographic model that was denser than that of the Clementine laser altimeter with a vertical accuracy of a few hundred meters. Its use was limited, however, by the highly variable accuracy.

* Corresponding author.
E-mail address: michael.k.barker@nasa.gov (M.K. Barker).

http://dx.doi.org/10.1016/j.icarus.2015.07.039

The Japanese SELENE (Kaguya) spacecraft, launched in 2007, carried onboard a laser altimeter (LALT) and a dedicated stereo imager (Terrain Camera). In its first three months of mapping, LALT collected 6.77×10^6 range measurements globally with an along-track shot spacing of ~ 1.6 km, a cross-track equatorial spacing of ~ 15 km, a radial uncertainty of ~ 4 m, and a horizontal uncertainty of ~ 77 m (Araki et al., 2009). From these data, Araki et al. (2009) produced the first polar topographic maps with complete coverage, and made improved estimates of the lunar figure from a spherical harmonic model complete to degree and order 359 on a quarter-degree grid. With its forward- and backward-looking channels, each Terrain Camera (TC) observation provided stereo images, thus yielding topographic information with which Haruyama et al. (2014) produced a global DEM with 10 m spatial posting and a vertical accuracy of 10 m or better.

Also launched in 2007, the Chinese Chang'e-1 spacecraft carried onboard a laser altimeter and stereo camera. Ping et al. (2009) processed over 3×10^6 range measurements from the laser altimeter with an along-track spacing of ~ 1.4 km and a cross-track equatorial spacing of ~ 7 km. They produced a global spherical harmonic topographic model complete to degree and order 360 with an absolute vertical accuracy of ~ 31 m on a quarter-degree grid and used it to estimate global shape parameters. The stereo camera onboard Chang'e-1 had a resolution of 120 m/pix and a ground-swath width of 60 km. Initial work has shown it can produce a near-global DEM with a grid pixel size up to 500 m and a horizontal accuracy of ~ 370 m (Liu et al., 2009).

The Indian Space Research Organization launched its Chandrayaan-1 spacecraft in October, 2008. Two of the 11 instruments onboard were the Lunar Laser Ranging Instrument (LLRI) and the Terrain Mapping Camera (TMC). The LLRI operated at a firing rate of 10 Hz with a range accuracy of $\leqslant 5$ m (Kamalakar et al., 2009). The TMC had a spatial resolution of 5 m and a 20 km ground-swath width from the nominal orbit altitude of 100 km. Recent work on a geometric correction model for the TMC achieved an RMS positional error of ~200 to 300 m (Radhadevi et al., 2013).

The Lunar Orbiter Laser Altimeter (LOLA) onboard the Lunar Reconnaissance Orbiter (LRO) has collected over 6.5×10^9 measurements of global surface height with a vertical precision of ~10 cm and an accuracy of ~1 m (Mazarico et al., 2013). With such highly accurate global coverage, the resulting topographic map has become the reference geodetic framework for the lunar community and has led to the highest resolution and most accurate polar digital elevation models (DEMs) to date. Also onboard LRO is the LRO Camera (LROC) consisting of a Narrow Angle Camera (NAC) and a Wide Angle Camera (WAC). The NAC is capable of taking stereo images with a resolution of 0.50 m and a cross-track swath width of 5 km. The WAC has a nadir resolution of 75 m/pix at visible wavelengths and a 60 km swath width, which allows stereo models to be produced with images from subsequent orbits. Scholten et al. (2012) used 17 months of WAC data to make the GLD100, a near-global DEM covering latitudes within $\pm 79°$ with an effective horizontal resolution ~1 km and a mean vertical accuracy better than 20 m globally.

The ability of laser altimeters to obtain global measurements independent of solar illumination conditions provides an advantage over passive stereoscopic imaging, particularly at high latitudes ($>60°$) where such imaging is hindered by low solar incidence angles and permanent shadow. In addition, laser altimetry provides a more accurate geodetic framework to which stereo models can be controlled. On the other hand, stereo imaging can provide denser surface coverage than laser altimetry, especially near the equator. With the ~18,000 LRO orbits considered in this paper, the typical equatorial gap width between LOLA groundtracks is ~500 m. This cross-track spacing represents a significant improvement over all the previous lunar-orbiting laser altimeters, but gaps in the LOLA coverage as wide as a few km still persist near the equator due to the very narrow cross-track width of the individual LOLA profiles. Thus, the LOLA altimetric dataset can benefit from the extensive cross-track coverage provided by the SELENE TC imagery.

Here we present the results of an effort to improve the LOLA coverage by incorporating topographic information from the independently-derived and highly complementary TC dataset. This dataset was controlled with an older version of the LOLA data geolocated with a gravity field made prior to the Gravity Recovery and Interior Laboratory mission (GRAIL; Zuber et al., 2013). In this study, we co-register the TC data to the newer, more accurate GRAIL-based LOLA geodetic framework, yielding 3–4 m root-mean-square (RMS) elevation residuals and increasing the fraction of residuals <5 m from ~50% prior to registration, to ~90% after registration. The goal of this work is to produce the most complete global terrain model of the lunar surface while preserving the geodetic accuracy of the LOLA data, by merging both high-resolution datasets. In addition to having many geophysical and exploration applications, the merged product will improve the orthorectification and co-registration of diverse lunar datasets to the latest LRO/LOLA/GRAIL geodetic system without the gaps normally present between LOLA groundtracks.

The outline of this paper is as follows. In Section 2, we describe the datasets used in this study. In Section 3, we explain the algorithm for co-registration of the datasets. The results of the co-registration are presented in Section 4, and the merged product, designated as "SLDEM2015" (SELENE and LRO DEM 2015), is examined in more detail in Section 5. Finally, we summarize and make concluding remarks in Section 6.

2. Description of the data

2.1. LOLA data

LRO entered lunar orbit in June 2009 followed by a commissioning phase during which the spacecraft had a $\sim 30 \times 200$ km polar orbit with periapsis near the south pole. In September 2009, the spacecraft moved into a nearly circular 50 km, 2-h orbit for the nominal mapping phase. In December 2011, it was moved into a quasi-stable elliptical orbit similar to the commissioning orbit.

In this study, we use all LOLA data through the Extended Science Mission Phase 9 (ending July 18, 2013). Orbit determination was performed with the lunar gravity field GRGM900B from the GRAIL mission (Zuber et al., 2013; Lemoine et al., 2014). With the GRAIL gravity field, the accuracy of the LRO reconstructed trajectory is ~ 10 m in total position and ~0.5 m vertically (Mazarico et al., 2013). Following the conventions set by the LRO project, we use the lunar DE421 ephemeris (Williams et al., 2008) with planetocentric coordinates expressed in the mean-Earth/polar-axis system and a reference radius of 1737.4 km.

LOLA is a time-of-flight laser altimeter operating at a firing rate of 28 Hz (Smith et al., 2010b). A diffractive optical element splits the laser beam into 5 separate far-field spots which form a cross pattern on the surface rotated by 26 ° with respect to the along-track direction. From the nominal primary mission mapping orbit altitude of 50 km, successive shots are separated by ~57 m on the surface and the 5-spot pattern is ~50 m in diameter, giving a cross-track separation of ~11 m between the 5 ground tracks and an along-track separation of ~10 m between spots. On the lunar night side, the instrument's thermal blanket contracts, pulling the beam expander out of alignment with the receiver telescope (mostly in the cross-track direction), typically resulting in returns from two of the five spots and an effective rate 40% of

the nominal day side rate of 140 measurements per second (Smith et al., 2010a).

2.2. Terrain Camera data

The TC was a push-broom stereo imager with two separate telescopes pointing 15° fore and aft of the Kaguya spacecraft (Haruyama et al., 2008). Hence, stereo observations could be acquired in a single orbit. Each telescope had its own one-dimensional CCD camera with a resolution of 10 m/pixel in the 100 km nominal mapping orbit. From this altitude, the camera's nominal ground swath width was ~1° (30 km). The global TC DEM dataset (SLDEM2013) is a mosaic of many different ground swaths typically several tens of degrees long in latitude, acquired from different orbits throughout the mission period. Further details can be found in Haruyama et al. (2014). SLDEM2013 is archived in separate $1^\circ \times 1^\circ$ tiles on the SELENE Data Archive (http://l2db.selene.darts.isas.jaxa.jp/archive/index.html.en). In this study, we use the 43,200 tiles covering latitudes within ±60°. The LOLA data coverage is sufficiently dense for most purposes at latitudes outside this range.

During the SELENE mission lifetime (November 2007 to June 2009), the TC acquired stereo imagery for over 99% of the surface (Haruyama et al., 2012). Because of extensive shadowing, LOLA data were exclusively used within 3° of the poles. At lower latitudes, in those areas where TC did not observe or where the images were otherwise dominated by shadows, data from the Multiband Imager (MI) were used. The MI was a visible to near-infrared color image sensor on Kaguya with a ground swath width of 19.3 km and a resolution of 20 m/pixel in the visible (Haruyama et al., 2008; Ohtake et al., 2008). Since the MI bands were forward or aft looking, they provided stereo pairs with a maximum oblique angle of ±5.5° between 415 nm and 900 nm band images. Due to the lower pixel resolution and oblique angles, the height resolution of MI DEMs is theoretically ~1/6 that of the TC DEMs.

The effective horizontal resolution of the TC DEM dataset is lower than its posting resolution of 10 m due to the inherent difficulties of stereophotogrammetry. To estimate the effective horizontal resolution, we randomly selected one tile within each of the 192 $15^\circ \times 15^\circ$ patches covering the study area, thereby sampling a wide range of terrains. Each tile was down-sampled to 2048, 1024, 512, 256, and 128 pixels per degree (ppd; corresponding to ~15, 30, 60, 120, and 240 m at the equator), and then processed with the full co-registration procedure described in Section 3. Fig. 1 shows the results as a box-plot of final RMS vertical (i.e., height or radial) residual between the fully co-registered TC and LOLA data as a function of tile resolution. Each box represents the statistics of the residuals from the ~13,000 unbinned LOLA profile segments passing through the selected TC tiles. There is a sharp increase in RMS below ~256 ppd (~120 m at the equator) and a global minimum at 512 ppd (~60 m at the equator). Since the resolution of the LOLA spots is much smaller than these scales, the behavior observed in Fig. 1 likely indicates that the effective resolution of the TC data is ~256 to 512 ppd. Indeed, the power spectra of these tiles show a cut-off at ~100 to 200 m with nearly scale-free noise dominating at wavelengths ≲100 m. To avoid over-smoothing the TC data, we adopt 512 ppd as the effective resolution. With this value each down-sampled pixel is, on average, roughly the size of the LOLA five-spot footprint.

3. TC-to-LOLA co-registration

Errors in the TC tiles result from imperfect knowledge of the Kaguya orbit, as well as errors in camera pointing, focal length, flat-field, distortion, and jitter. Offsets in the LOLA profiles are due largely to orbit uncertainties and errors in the laser boresight model. To isolate these error sources, we follow a two-step approach when co-registering the TC tiles to the LOLA data. In step (1), we derive a 5-parameter coordinate transformation between every TC tile and the full resolution LOLA data in that tile (unbinned point cloud with ~100,000 points). Given the large number of individual profiles (typically ~70 per tile), we expect the LRO/LOLA orbital and pointing errors to average out to very nearly zero in any given tile given they are uncorrelated over the ~4 years of acquisition. Thus, the tile-averaged transformation parameters compensate predominantly for the Kaguya/TC orbital, pointing, and camera model errors. In step (2), we fit a 3-dimensional (3D) offset to each LOLA profile segment in the transformed TC tile. These offsets reflect primarily the LOLA geolocation errors described above with a secondary contribution from Kaguya/TC errors not completely removed by the transformation in step (1) due to the low number of degrees of freedom.

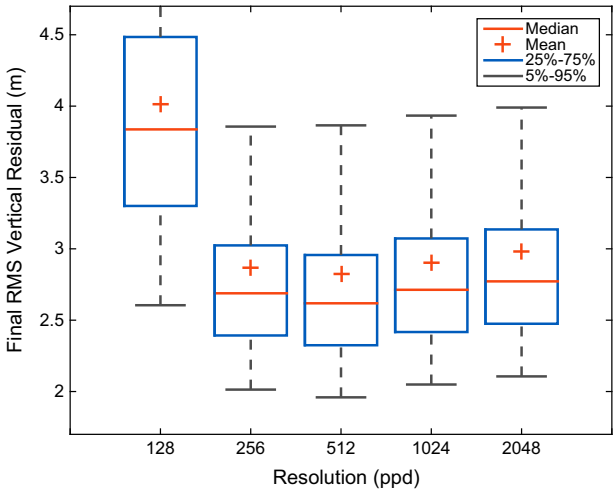

Fig. 1. Box-plot of final RMS vertical residual between ~13,000 individual unbinned LOLA profile segments and TC tiles at various resolutions after applying the full co-registration procedure described in Section 3. The minimum RMS occurs at a resolution of 512 ppd indicating the effective resolution of the TC data.

The tile-averaged transformation of step (1) includes a 3D translational offset $(\Delta x,\Delta y,\Delta z)$ in the horizontal (longitude, latitude) and vertical directions, and two planar tilts (t_x,t_y) in the horizontal directions relative to each tile's center longitude and latitude (x_0, y_0):

$$x' = x + \Delta x \tag{1}$$

$$y' = y + \Delta y \tag{2}$$

$$z' = z + \Delta z + t_x(x - x_0) + t_y(y - y_0) \tag{3}$$

We employ a bounded downhill simplex minimization algorithm (Lagarias et al., 1998) with multiple random starting locations that minimizes the RMS vertical residual after removal and down-weighting of outlier points. For robustness, the planar tilts are initially fixed at zero to obtain a first guess of the translational offsets (limited to ±300/30 m horizontally/vertically). Then, to solve for all 5 parameters simultaneously, the translational offset bounds are re-centered on the estimates just derived and the bound intervals decreased to ±120/10 m, while the tilt bounds are set to $\pm 15\ \mathrm{m\ deg^{-1}}$. A set of 5 random initial parameter vectors within these bounds is used for the simplex starting locations. The solution with the minimum RMS of these 5 vectors is retained. The process is repeated with at most 10 more random starting

locations, stopping when the standard deviation of the saved RMS minima is <0.2 m. Then, the solution with the overall smallest RMS becomes the final best-fit solution.

We use Huber weighting (Huber, 1981) when computing the RMS values in order to avoid convergence error and instability due to outliers. The residuals are assigned a weight $w(r) = \min(1.0, 3\sigma/|r|)$, where r is the residual and σ is the standard deviation of residuals. Each LOLA profile in a tile is further weighted inversely proportional to its number of points, so that profiles with more points do not adversely dominate the fit. This is done because positioning errors of altimetric points in one track segment (~20 s for the 1° tiles) are very correlated since they are primarily due to orbit error, and such errors are just as likely in a 1000-point segment as in a 100-point segment.

A similar fitting algorithm is used in step (2) to find the 3D offsets for each LOLA profile segment, again minimizing the Huber-weighted vertical residual RMS. The transformation equations are identical to Eqs. (1)–(3) except the tilts are zero ($t_x = t_y = 0$). The maximum number of points in each daytime profile segment is ~2600. Because of the thermal blanket anomaly, the maximum number of points in each nighttime profile segment is ~1000. The initial parameter bounds are ±100 m in the horizontal directions and ±30 m in the vertical direction.

The co-registration procedure does not explicitly enforce continuity between adjacent tiles. However, we find that after the co-registration (see Section 5.5), most discontinuities across tile boundaries (i.e., seams) have magnitudes less than the RMS residuals within the tiles themselves. To reduce the presence of the largest seams, we replace the most poorly fit ~1% of tiles with the original LOLA-only DEMs (without the step (2) profile offsets) with interpolation to fill gaps.

We tested the co-registration algorithm on a simulated dataset with artificial noise and with known input parameters. The dataset consisted of the 192 tiles used in Fig. 1, which cover a range of terrains. Artificial LOLA profiles were created by sampling the full resolution version of each TC tile at the locations of the LOLA points. To simulate the orbital errors in each profile, known 3D offsets were created from a normal distribution with zero mean and standard deviation of 10/10/1 m in the $X/Y/Z$ directions (i.e., longitude/latitude/vertical). Artificial data, simulating the TC tile after stereo processing, were created by applying 3D offsets and tilts to each full-resolution tile, adding vertical noise, and down-sampling to 512 ppd. The tile-averaged offsets were drawn from a normal distribution with zero mean and standard deviation of 20/20/2 m in $X/Y/Z$. The tilts were drawn from a normal distribution with zero mean and standard deviation of 2 m deg^{-1}. The vertical noise was also normally distributed, with zero mean and standard deviation of 30 m. This vertical noise distribution was chosen to yield final RMS values close to those actually observed. This simulation showed that the parameters can be recovered with a precision much smaller than the pixel size of 60 m at the equator. The mean error and standard deviation in the recovered tile-averaged offsets was $\sim 0 \pm 2$ m horizontally and 0.0 ± 0.2 m vertically, and the mean error in the recovered tilts was $\sim 0.0 \pm 0.6$ m deg^{-1}. The mean error in the recovered profile offsets was $\sim 0 \pm 8$ m horizontally and 0.0 ± 0.6 m vertically.

4. Results

4.1. Step 1: Tile-averaged transformation

The co-registration procedure described in Section 3 was applied to the 43,200 TC tiles and $\sim 4.5 \times 10^9$ LOLA measurements in the study area. The tile-averaged translational offsets were typically at the sub-pixel level with median absolute values of 8.3/18.2/1.6 m in $X/Y/Z$. Because their distributions have relatively large tails (see Fig. 2), the RMS spread (32.7/70.3/4.2 m) is not indicative of half the central 68% interval (hereafter referred to as σ) as the case with a perfect Gaussian distribution would be. This is not unexpected given the presence of systematic effects like spacecraft orbit and attitude reconstruction errors. The actual values of σ in $X/Y/Z$ are 12.1/16.8/1.9 m. The distribution of tilts is shown in Fig. 3. The median absolute values in X/Y are 1.6/1.2 m deg^{-1} and $\sigma = 2.4/1.9$ m deg^{-1}. The fact that the spread in the offsets and tilts is much larger than the errors of the recovered parameters in the tests in Section 3 suggests that the offsets reflect actual data positioning errors. Indeed, a map of the offsets shows a clear consistency of neighboring tile adjustments which are highly correlated with the original TC acquisition ground swaths with their own particular orbital, pointing, and camera errors at their respective observation times.

The offset distributions are not centered on zero, but instead indicate a global median shift of the TC coordinate system by about 3 m eastward, 16 m northward, and 1 m outward in the vertical direction. We verified such offsets on a subset of the data (the same 192 tiles used in Fig. 1) using the *pc_align* program of the Ames Stereo Processing Pipeline (Beyer et al., 2014). This program uses an iterative closest point matching algorithm to derive the transformation parameters between two point clouds. The shifts obtained with *pc_align* agreed with those obtained by our method. We note that the shifts are significantly smaller than the pixel size.

Fig. 4 shows the distribution of unweighted RMS vertical residual between all of the unbinned LOLA points and each TC tile. The open (blue) histogram and lower (blue) curve show the initial probability distribution and cumulative distribution, respectively. The solid (red) histogram and upper (red) curve show the same quantities after applying the tile-averaged transformation in step (1). The median RMS residual decreases from 4.9 m to 3.4 m while the 90th percentile decreases from ~10 m to 5 m. The long tail toward high RMS is due primarily to problems in the Kaguya orbit and attitude reconstruction, and the inclusion of the lower resolution MI DEMs in the production of SLDEM2013. These anomalies tend to stand out as coherent vertical stripes in the spatial distribution shown in Fig. 5.

The top panel in Fig. 5 shows the initial RMS vertical residual spatial distribution while the bottom panel shows the final RMS distribution after applying the tile-averaged transformation in step

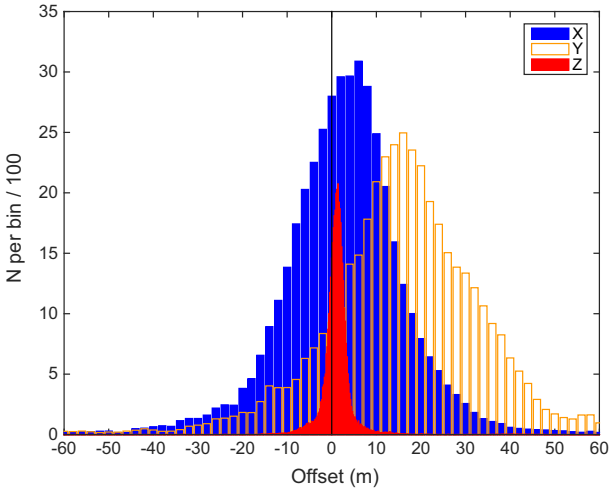

Fig. 2. Distribution of X, Y, and Z (longitude, latitude, and vertical) offsets for the tile-averaged transformation in step (1). The X and Y bin size is 2 m and the Z bin size is 0.2 m. The median absolute values in $X/Y/Z$ are 8.3/18.2/1.6 m and $\sigma = 12.1/16.8/1.9$ m.

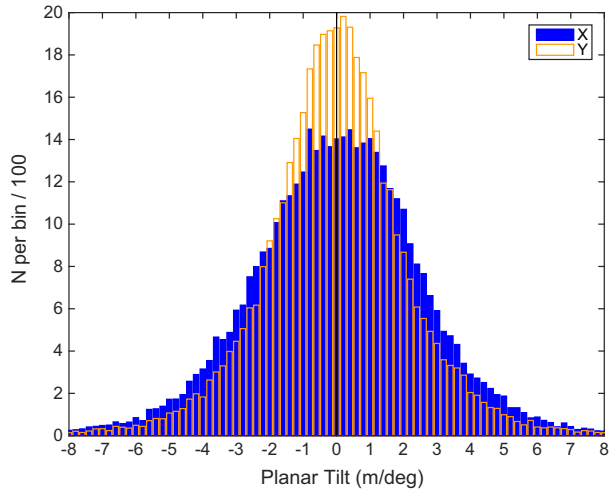

Fig. 3. Distribution of planar tilts in the X and Y (longitude, latitude) directions for the tile-averaged transformation in step (1). The median absolute values in X/Y are $1.6/1.2\text{mdeg}^{-1}$ and $\sigma = 2.4/1.9\text{mdeg}^{-1}$.

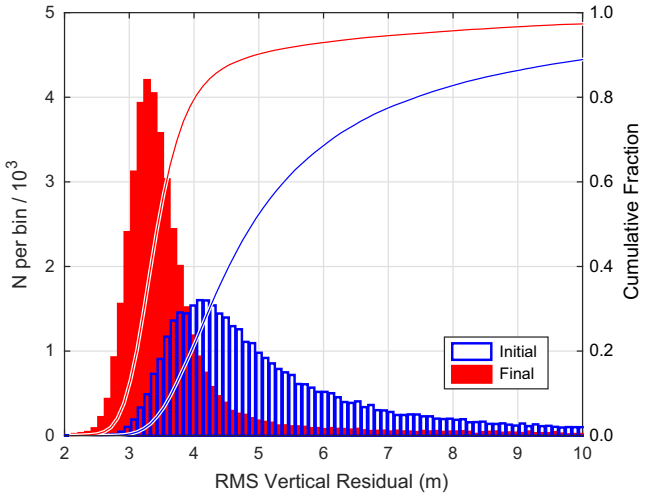

Fig. 4. Distribution of RMS vertical residuals between unbinned LOLA points and all 43,200 TC tiles between latitudes ±60°. The open (blue) histogram and lower (blue) curve show the initial probability distribution and cumulative distribution, respectively. The solid (red) histogram and upper (red) curve show the same after applying the tile-averaged transformation in step (1). The median decreases from 4.9 m to 3.4 m while the 90th percentile decreases from ~10 m to 5 m. The RMS residual spatial distribution is shown in Fig. 5. (For interpretation of the references to color in this figure legend, the reader is referred to the web version of this article.)

(1). Two areas with particularly high residuals include the South Pole Aitken basin (SPA; 45–60°S, 140–210°E) and the western edge of Orientale basin (45°S–15°N, 230–260°E). The large errors in SPA are due to the lower-resolution MI DEMs, while in Orientale, reaction wheel troubles on Kaguya led to worse orbit reconstruction on those observation dates. The tile-averaged transformation also significantly improved some areas on the far side, especially between ±30° latitude and 180–200°E longitude. These areas have initial RMS residuals of ~8 to 18 m, and have less vertically-oriented shapes than the regions mentioned previously. We attribute the initially high residuals in these far side areas to differences in gravity field models used by the reference LOLA data; SLDEM2013 was referenced to LOLA data based on pre-GRAIL gravity field LLGM-2 whereas in this work we use the much higher resolution and more accurate GRAIL GRGM900B (see Mazarico et al. (2013) for discussion).

4.2. Step 2: Individual LOLA profile offsets

Fig. 6 shows the distributions of the best-fit 3D offsets for the ~3 million LOLA profiles (each ~1° long in latitude). These offsets have median absolute values of 9.3/7.0/0.6 m, RMS spreads of 20.6/22.8/1.6 m, and $\sigma = 14.2/10.5/1.0$ m. The horizontal offsets are dominated by errors in the LOLA boresight model and LRO orbital errors while the vertical offsets are dominated by orbital errors. A smaller contribution to the offsets comes from errors in the TC-to-LOLA transformation model, TC camera model, Kaguya orbit, and misalignment of the tile boundaries with the TC ground-swaths. Excluding profiles with final RMS values >3.4 m (i.e., the 90th percentile), the RMS spread decreases to 13.8/12.0/0.9 m. The magnitude of these offsets agrees with orbit overlap results from precision orbit determination for LRO (Mazarico et al., 2013). The asymmetric shape of the X-offset distribution results mainly from the interplay of 3 time-varying effects: the semi-annual yaw flips of the spacecraft, the night-side thermal blanket anomaly (Smith et al., 2010b), and a small offset in the boresight model from the true value. A detailed analysis of these effects is beyond the scope of the present study, but is the subject of current work.

Fig. 7 shows the distribution of RMS vertical residual between the LOLA profile segments and the corresponding adjusted TC tiles. The open (blue) histogram and lower blue curve show the initial probability distribution and cumulative distribution, respectively, after applying the tile-averaged transformation in step (1) but before the 3D profile offsets in step (2). The solid (red) histogram and upper red curve show the same after applying the 3D profile offsets in step (2). The median RMS residual decreases from 3.2 m to 2.6 m while the 90th percentile decreases from ~5.0 m to 3.4 m.

5. Discussion

5.1. SLDEM2015: The merged LOLA + TC product

With the transformation parameters in hand, we can create SLDEM2015, the new LOLA + TC merged product. First, we apply the inverse transformation to bring the TC tiles to the LOLA geodetic system, and then down-sample them to 512 ppd. Next, we make a LOLA-only map by applying the profile offsets to individual LOLA tracks to remove orbital/pointing errors, and then bin the data at 512 ppd with a median filter. Typically, empty pixels in the LOLA-only map would be interpolated with a continuous curvature surface. Now it is possible to fill the empty pixels with the corresponding pixels of the geodetically-controlled TC tiles.

Fig. 8 compares 3 different DEMs of the region around the landing site of the Chang'e 3 spacecraft: Fig. 8a shows LOLA data alone, after continuous curvature interpolation between ground tracks. Fig. 8b is our new SLDEM2015 merged product. Fig. 8c shows the GLD100 DEM, which was produced from Lunar Reconnaissance Orbiter Camera (LROC) Wide Angle Camera (WAC) stereo imagery (Scholten et al., 2012).

The SLDEM2015 (Fig. 8b) reveals surface detail not sampled by the LOLA ground-tracks (e.g., the crater at [45°N, −19.5°E]). It gives an elevation of −2628 m for the Chang'e 3 site, using the location (44.1213°N, −19.5115°E) derived from LROC Narrow Angle Camera images (Wagner et al., 2014). The LOLA-only DEM gives an elevation 6 m lower than SLDEM2015. The GLD100 yields an elevation 11 m lower than SLDEM2015 (Wagner et al., 2014), but within the ~20 m vertical uncertainties of the GLD100 (Scholten et al., 2012). We note that the effective horizontal resolution of the GLD100 is ~1 km (Scholten et al., 2012), which is consistent with the sizes of the smallest craters visible in Fig. 8c.

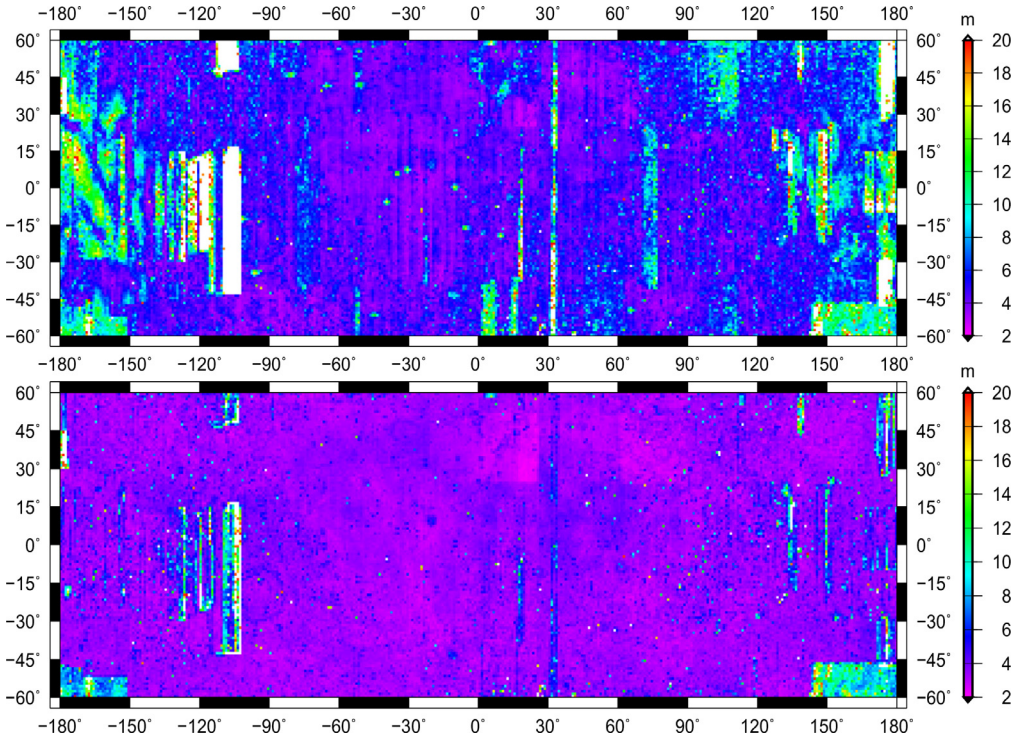

Fig. 5. Top: Spatial distribution (in cylindrical projection) of initial RMS vertical residual between TC tiles and unbinned LOLA data. Bottom: The same, but after applying the tile-averaged transformation in step (1). Fig. 4 shows histograms of these map values. Regions of anomalously high RMS in the bottom panel are due to errors in Kaguya orbit and attitude reconstruction, and the inclusion of coarser stereo models from MI.

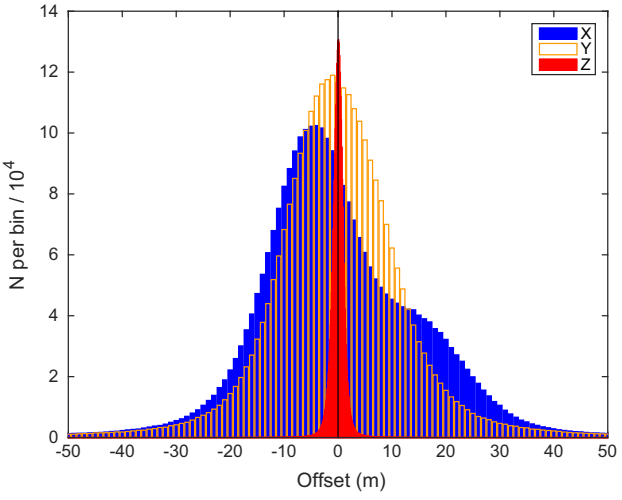

Fig. 6. Distribution of *X*, *Y*, and *Z* (longitude, latitude, and vertical) offsets for the ~3 million LOLA profile segments in step (2). The *X* and *Y* bin size is 1 m and the *Z* bin size is 0.1 m. The median absolute values in *X*/*Y*/*Z* are 9.3/7.0/0.6 m and $\sigma = 14.2/10.5/1.0$ m. The horizontal offsets are dominated by errors in the LOLA boresight model and LRO orbital errors while the vertical offsets are dominated by orbital errors. A smaller contribution to the offsets comes from errors in the TC-to-LOLA transformation model, TC camera model, Kaguya orbit, and misalignment of the tile boundaries with the TC ground-swaths.

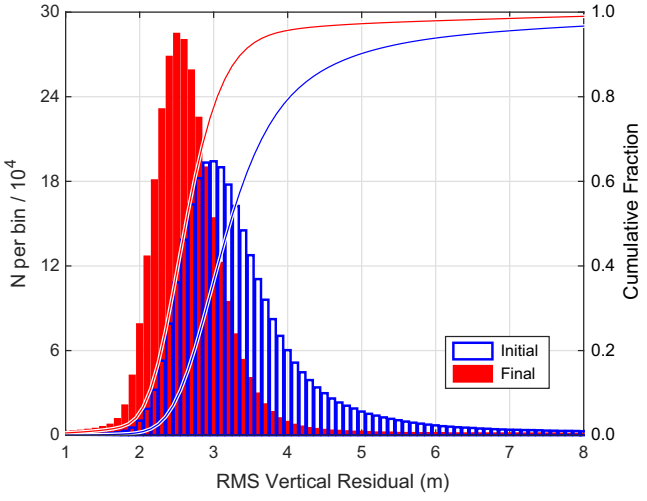

Fig. 7. Distribution of RMS vertical residual between all ~3 million individual LOLA profile segments and the corresponding co-registered TC tiles between latitudes ±60°. The open (blue) histogram and lower (blue) curve show the initial probability distribution and cumulative distribution, respectively, after applying the tile-averaged transformation in step (1) but before the 3D profile offsets in step (2). The filled (red) histogram and upper (red) curve show the same after applying the 3D profile offsets in step (2). The median RMS residual decreases from 3.2 m to 2.6 m while the 90th percentile decreases from ~5.0 m to 3.4 m. (For interpretation of the references to color in this figure legend, the reader is referred to the web version of this article.)

Fig. 9 shows elevation residuals between the fully co-registered TC and LOLA 512 ppd maps over a small region. Areas of high slopes, such as the far side highlands and crater walls, tend to have larger absolute residuals than regions of low slopes, such as the near side maria and crater floors, likely due to higher roughness at the pixel scale. In addition, horizontal ripples with a characteristic wavelength of ~1.2° and amplitude ~1.5 m are visible over flat terrain. These ripples are coherent over tens of degrees in longitude, spanning multiple TC ground-swath acquisitions, although their phase drifts somewhat. The amplitude of these ripples is less than the global median final step (1) RMS of 3.4 m. Therefore, caution should be exercised when interpreting features of vertical extent less than the final step (1) RMS residual, whose map is shown in the lower panel of Fig. 5.

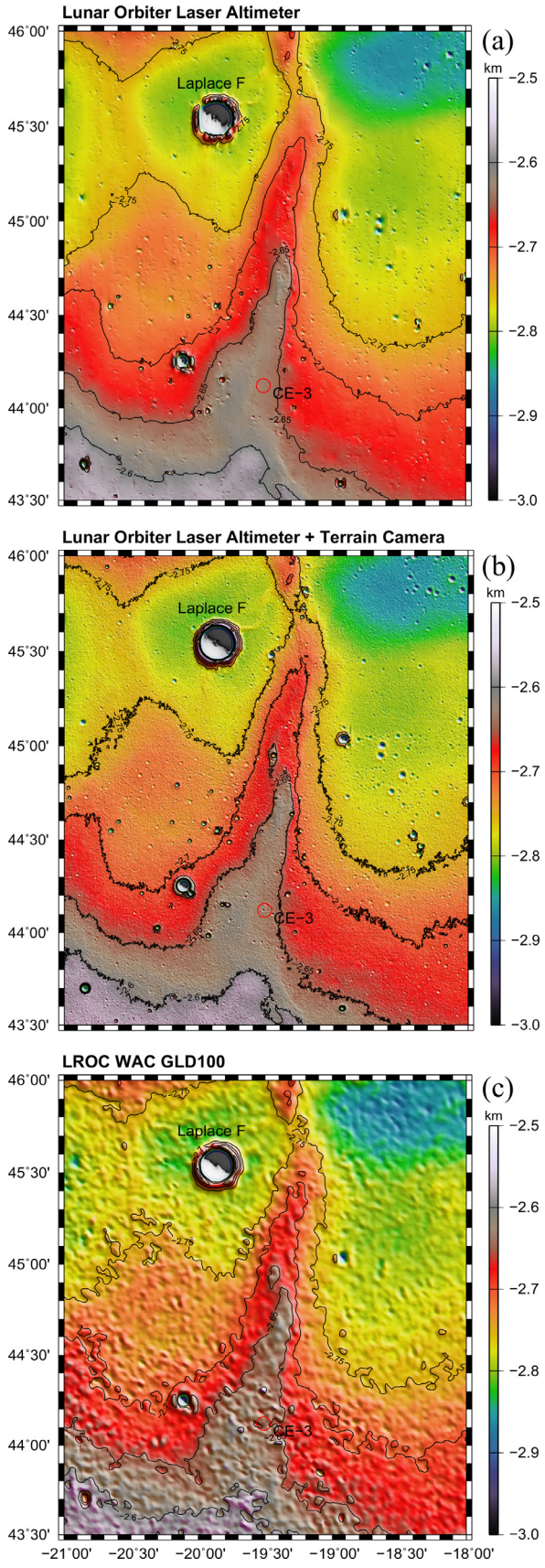

Fig. 8. Comparison of DEMs of the Chang'e 3 landing site (labeled red circle) in Mercator projection. (a) LOLA DEM with continuous curvature interpolation to fill gaps between tracks. (b) SLDEM2015 merged DEM where the fully co-registered TC DEM is used to fill the gaps. (c) LROC WAC GLD100 DEM. (For interpretation of the references to color in this figure legend, the reader is referred to the web version of this article.)

As an additional check on SLDEM2015, we computed the elevations at the 5 laser ranging retro-reflector sites (Apollo 11, 14, 15, and Lunokhod 1 and 2) using the coordinates derived from lunar laser ranging (LLR) data (Williams et al., 2008; Murphy et al., 2011). Table 1 lists the elevation residuals at these sites where we have subtracted the LLR elevation from the DEM elevation for the GLD100, SLDEM2013, SLDEM2015, and LOLA-only DEMs. The LLR elevation includes the static tidal bulge of the Moon, but not the height of the retro-reflectors above the surface.

As can be seen from Table 1, the co-registration procedure has improved the agreement between the TC-based elevations and LLR-based elevations, decreasing the RMS residual from 3.97 m for SLDEM2013 to 2.44 m for SLDEM2015. This highlights the fact that there is some noise of amplitude ~2 to 3 m remaining in SLDEM2015. This noise may arise from unmodeled errors in the Kaguya orbit and attitude reconstruction, as well as spacecraft vibration (i.e., jitter), image compression (Haruyama et al., 2008), and stereo image correlation difficulty if too few morphologic or albedo features are visible. At some locations, the noise from such sources may be comparable to or greater than the real topographic variation. This may be why the TC DEM gives somewhat less accurate elevations at these particular sites than the LOLA-only DEM, which has an RMS residual of 0.65 m. Finally, we note that the more recently derived LLR retro-reflector coordinates, based on the DE430 ephemeris (Williams et al., 2013), differ from the older ones by <0.30 m radially and <1.7 m horizontally, and would change the elevation residuals in Table 1 by <0.50 m and the RMS values by <0.12 m.

5.2. Accuracy of interpolation

As explained previously, the LOLA-only maps use interpolation to fill in gaps in coverage. The elliptical orbit in the extended science mission of LRO has led to better coverage in the southern than in the northern hemisphere so that these gaps are typically ~500 m wide near the equator and ~50/100 m wide at −80°/+80° latitude. The full co-registration of the LOLA and TC datasets allows us to quantify the interpolation errors in the LOLA-only DEM. Such errors may be relevant to the results and interpretation of other studies based on that DEM, particularly those focused on scales comparable to or less than the typical gap size (e.g., crater-count studies).

If we take the co-registered TC data within the gaps as "truth," then we can estimate the topographic errors introduced by this interpolation. In reality, the co-registered TC-only map is not perfect truth, so we must remove the contribution of its own errors to the difference map. To that end, we subtracted the median residual between the co-registered TC-only and LOLA-only maps for non-interpolated pixels from that of interpolated pixels in square bins 16 pixels on a side, and then took the absolute value of that quantity for each bin. The result, shown in Fig. 10, is the median absolute interpolation error of the LOLA-only 512 ppd map. Some artifacts due to errors in the TC DEMs remain (especially in SPA), but overall this map reflects the effects upon the interpolation accuracy of surface slope (at baselines near the pixel size) and gap size, which tends to increase toward the equator. The LOLA interpolation has a typical error of <1 m over the maria. This is consistent with our analysis of the retro-reflector sites (Section 5.1 and Table 1), which showed sub-meter agreement with the LOLA-only and LLR-based elevations. Over the highlands, the interpolation errors are higher, vary much more than over the maria, and tend to increase toward the equator as the average gap width concurrently increases. The maria are so flat that even the largest gaps have small errors in interpolation. Hence, the maria's interpolation accuracy depends little on latitude.

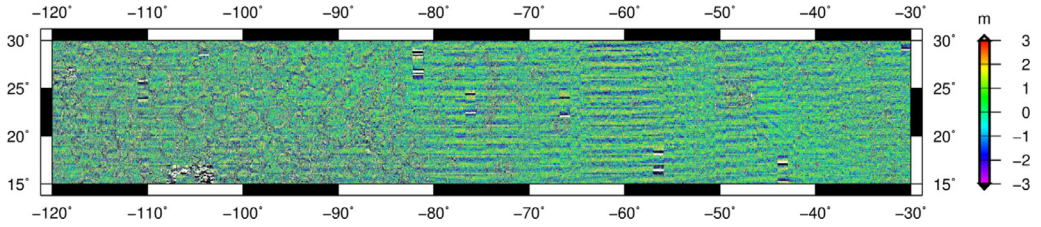

Fig. 9. A cut-out of the residual map after the full co-registration. Crater walls tend to have larger residuals than crater floors. Horizontal ripples with a characteristic wavelength of ∼1.2° and amplitude ∼1.5 m are visible over flat terrain. These ripples are coherent over tens of degrees, though the phase drifts somewhat, and span multiple orbits and TC ground-swaths, but their amplitude is smaller than the final step (1) RMS vertical residual.

Table 1
Elevation residuals at the retro-reflector sites defined as DEM elevation – LLR elevation.

Site name	GLD100 (m)	SLDEM2013 (m)	SLDEM2015 (m)	LOLA (m)
Apollo 11	−3.91	−2.71	−2.81	0.08
Apollo 14	13.26	3.26	−0.13	−0.08
Apollo 15	0.26	−0.01	−0.59	−0.59
Lunkd. 1	−16.84	−6.54	−4.39	−1.22
Lunkd. 2	−10.89	4.27	1.48	−0.49
RMS	10.90	3.97	2.44	0.65

5.3. Spherical harmonics

In addition to gridded map products, the LOLA data are also released as spherical harmonic coefficients. Expansions to progressively higher degree and order have been produced since the first LOLA data release (Neumann, 2010). With the higher degrees capturing the shorter-wavelength features of the topography, we can expect differences between the expansions of the LOLA-only and SLDEM2015 datasets to grow with increasing degree. We constructed global topographic maps at 512 ppd, complementing the ±60° maps of Section 5.1 with polar LOLA data for higher latitudes, and used the SHTOOLS software library (http://shtools.ipgp.fr) to obtain $L = 2500$ expansions. The RMS power of their coefficient differences is <1% at low degrees ($L \sim 400$, equivalent to ∼14 km at the equator) and reaches ∼10% at $L \sim 1800$ (∼3 km) and ∼15% at $L \sim 2500$ (∼2 km). The mean radius of SLDEM2015 inferred from the C_{00} coefficient is 1737.1512 km, or 248.8 m below the reference radius of 1737.4 km. This is 10 cm smaller than the mean radius derived from the LOLA-only DEM. The first-degree coefficients yield a center-of-mass/center-of-figure (COM/COF) offset vector of (−1.7752, −0.7311, 0.2399) km in the mean-Earth/polar-axis coordinate system, corresponding to a total displacement of 1.9347 km in the direction of (7.12218°N, 202.38310°E). The COM/COF offset vector components are within 3 m of previous estimates based on lower-degree expansions of 6.77×10^6 topographic returns from the SELENE Laser Altimeter (Araki et al., 2009) and 2×10^9 returns from LOLA (Smith et al., 2010a). The pixel with the highest elevation in SLDEM2015 is located at (5.40918°N, 201.36816°E) with a height of 10783.3 m. The lowest elevation lies at (−70.36035°N, 188.70410°E), outside the area covered by SLDEM2015, but the LOLA-only map gives a height of −9129.3 m.

For many geophysical studies of the Moon, the analysis of the gravity data greatly benefits from the use of topography, in order to account for the expected contribution of the surface relief to the measured free-air gravity anomalies. In particular, many recent studies of the GRAIL gravity field (Zuber et al., 2013) made use of the Bouguer correction to study the Bouguer anomaly maps and learn about sub-surface mass anomalies (Wieczorek et al., 2013; Andrews-Hanna et al., 2013; Besserer et al., 2014). The Bouguer correction can be computed to high accuracy using the finite amplitude algorithm of Wieczorek and Phillips (1998). In the case of the Moon, an expansion order $n > 14$ is required to yield <1 mGal error at $L = 900$ (Wieczorek, 2007), so we used $n = 20$ to ensure full convergence of the series at $L = 2500$. The power spectrum of the LOLA-only vs. SLDEM2015 difference always lies well below the GRGM900C Bouguer spectrum (Lemoine et al., 2014) at all degrees, with a maximum ratio of ∼10% at $L \sim 550$ where the Bouguer power plateaus ("Bouguer break"). At that degree, the GRGM900C gravity field degree power is $\sim 7.5 \times 10^{-10}$, while the GRGM900C Bouguer degree power is $\sim 10^{-10}$ and the LOLA-only vs. SLDEM2015 difference degree power is $\sim 1 \times 10^{-11}$. At higher degrees, while the Bouguer spectrum increases, the difference spectrum remains nearly flat (their ratio grows from ∼10 at $L = 550$ to ∼42 at $L = 900$). This indicates that the longitudinal gaps in the LOLA coverage do not significantly affect the gravity-from-topography computation at degrees relevant to gravity studies, and that it is adequate to use the LOLA-only expansion with the GRAIL gravity fields.

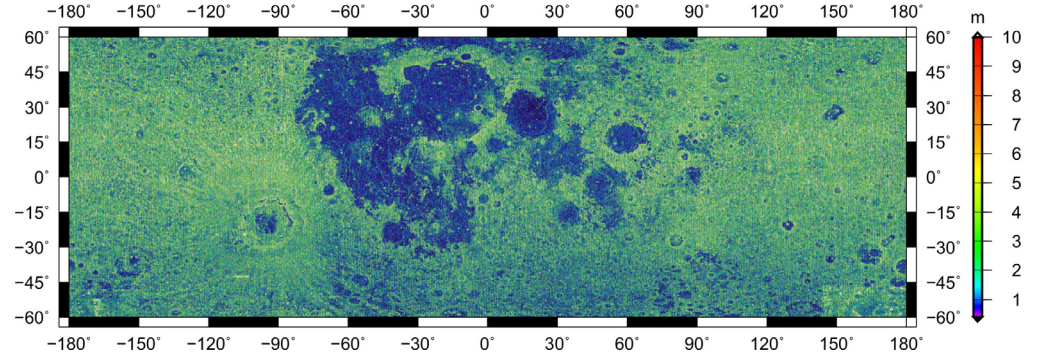

Fig. 10. A cylindrical projection map of the median absolute error of surface interpolation in gaps in the LOLA-only 512 ppd DEM. Interpolated pixels are more accurate over flat terrain, such as the near side maria, than over rough terrain, such as the far side highlands.

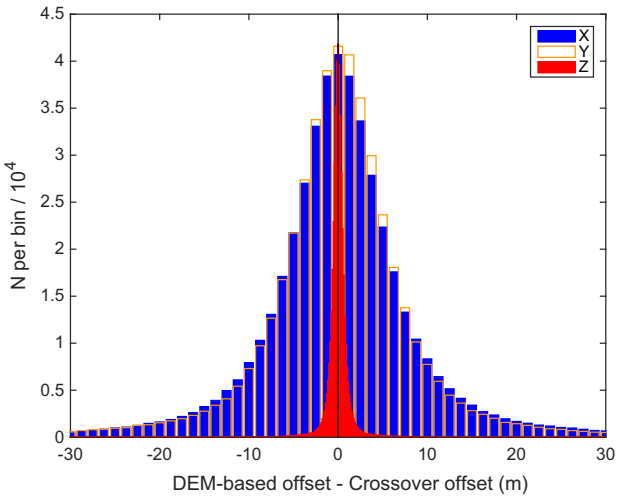

Fig. 11. Residuals between ~465,000 matched DEM-based pseudo-crossovers and LOLA-only crossovers. The *X* and *Y* bin size is 1.25 m and the *Z* bin size is 0.125 m. The median absolute values in *X*/*Y*/*Z* (longitude/latitude/vertical) are 4.2/4.0/0.4 m and σ = 6.8/6.4/0.6 m.

5.4. Crossovers

As described in Section 3 and in Section 4.2, the profile offsets derived in step (2) contain useful information on LRO/LOLA orbital and pointing errors. The difference between the step (2) offsets for any particular pair of profiles forms a DEM-based "pseudo-crossover". Pseudo-crossovers are of great interest for future studies to characterize the LRO/LOLA orbital errors, the LOLA boresight, and lunar tidal deformations (Mazarico et al., 2014), because the two nearly-meridional track segments do not have to actually intersect, greatly increasing the available number of crossovers. Before taking the differences, we remove long-wavelength trends in the *X*/*Y*/*Z* offsets within individual co-registered TC tiles because we focus on LOLA track segments that are close to each other. Then, we create nearly 9 million pseudo-crossovers by taking the pairwise differences between every profile's offset and its 3 closest neighbors. Finally, by considering their times and locations, we matched ~465,000 pseudo-crossovers with "real" LOLA-only crossovers (i.e., those for which the ground-tracks actually intersect) to which Mazarico et al. (2014) applied 3D offsets to minimize their vertical discrepancies.

Fig. 11 shows the distribution of residuals between the matched 3D offsets of the real and pseudo-crossovers. The median absolute residuals are 4.2/4.0/0.4 m, the RMS spread is 13.7/13.7/2.2 m, and σ = 6.8/6.4/0.6 m. The spread in these residuals reflects the combined random error in the pseudo-crossovers and the real crossovers. Therefore, this spread is an upper limit on the random error of the individual 3D profile offsets derived in step (2). This is consistent with the results of the tests in Section 3, in which the recovered profile offsets had spreads of 8 m and 0.6 m horizontally and vertically, respectively. The good agreement between both sets of crossovers opens the possibility for improving the spatial and temporal coverage of the real crossovers, which were limited by the polar orbit of LRO and the thermal blanket anomaly (Mazarico et al., 2014).

5.5. Seams

The co-registration procedure made no explicit constraints on the continuity between adjacent tiles. Hence, there will inevitably be discontinuities across tile boundaries after independent tile transformations. However, since the co-registration was based on the LOLA profiles, themselves continuous, the discontinuities should generally be small compared to other noise sources. To quantify the discontinuities, we computed the RMS pixel-by-pixel difference between the top and bottom row of vertically adjacent pairs of tiles, and subtracted from it the RMS difference between the top and next-to-top row to cancel out the local slope. This normalized RMS latitudinal boundary difference ($dRMS_{lat}$) should average out to zero in the absence of discontinuities. We find that the median $dRMS_{lat}$ is 1.1 m and 95% of the tiles have $|dRMS_{lat}| < 3.8$ m. Larger discontinuities tend to occur in tiles with poorer fits (e.g., those with higher fit RMS). Only ~4% of tiles have $|dRMS_{lat}|$ greater than their final step (1) RMS residual.

Defining a similar quantity, $dRMS_{lon}$, for the longitudinal discontinuities and repeating the above analysis shows that the median $dRMS_{lon}$ is 0.7 m and 95% of the tiles have $|dRMS_{lon}| < 6.6$ m, and ~10% of tiles have $|dRMS_{lon}|$ greater than their final step (1) RMS residual. The longitudinal discontinuities tend to be larger than the latitudinal ones because the left/right edges of the tiles may lie in different TC ground-swath acquisitions characterized by different offsets, whereas top/bottom neighboring tiles are more likely to have been acquired over the same Kaguya orbit.

To reduce the presence of the most noticeable seams, we adopt the expedient of replacing the most poorly fit tiles with the original LOLA DEMs (without the profile offsets) with interpolation to fill gaps. This applies to the 443 tiles (~1% of the total) with final step (1) RMS > 16 m.

6. Summary and conclusions

In this study, we have co-registered 43,200 TC DEM tiles to the LOLA geodetic framework to produce a combined topographic map of the Moon at a resolution of 512 ppd. The bulk of the co-registered TC tiles have vertical residual with the LOLA data of 3 to 4 m. The co-registered TC data were used to estimate and remove orbital and pointing errors (typically amounting to <10 m horizontally and <1 m vertically) from the LOLA altimetric profiles. By combining both datasets, gaps in the LOLA data can be filled without the need for interpolation. Given the high (~1 m) absolute vertical accuracy of the LOLA data found in orbit overlap analysis (Mazarico et al., 2013), we conclude the typical vertical accuracy of the resulting merged product is 3 to 4 m. This product, designated as SLDEM2015 and available from the Planetary Data System LOLA data node (http://imbrium.mit.edu/EXTRAS/SLDEM2015/) has many geophysical and cartographic applications in lunar science, as well as exploration and mission design. Studies requiring the high geodetic accuracy of the LOLA data and the excellent spatial coverage of the TC data will especially benefit from this merged data product.

Future work will focus on improved co-registration accuracy through the use of the original TC ground swath acquisitions because their boundaries do not generally align with the 1° × 1° tiles. A more sophisticated tile transformation that accounts for rotation, scale, and shear, and the use of the residual map to make additional spatially-varying non-parametric corrections, could also further improve the co-registration.

Acknowledgments

This work was supported by NASA's Lunar Reconnaissance Orbiter Project and Planetary Geology and Geophysics Program. We thank the SELENE (Kaguya) TC team and the SELENE Data Archive for providing the SELENE (Kaguya) data. SELENE is a Japanese mission developed and operated by JAXA. We also thank the LRO Mission Operations Center and LOLA science teams for

their hard work in producing the LOLA data used in this study. We are grateful to the anonymous reviewers for constructive feedback which improved the quality of this paper.

References

Andrews-Hanna, J.C., et al., 2013. Ancient igneous intrusions and early expansion of the Moon revealed by GRAIL gravity gradiometry. Science 339, 675–678. doi:10.1126/science.1231753.

Araki, H., et al., 2009. Lunar global shape and polar topography derived from Kaguya-LALT laser altimetry. Science 323, 897. doi:10.1126/science.1164146.

Archinal, B. et al., 2006. U.S. Geological Survey Open-File Report 2006-1367 <http://pubs.usgs.gov/of/2006/1367/>.

Baker, D.M.H., et al., 2012. The transition from complex craters to multi-ring basins on the Moon: Quantitative geometric properties from Lunar Reconnaissance Orbiter Lunar Orbiter Laser Altimeter (LOLA) data. J. Geophys. Res. (Planets) 117, 0. doi:10.1029/2011JE004021.

Besserer, J., et al., 2014. GRAIL gravity constraints on the vertical and lateral density structure of the lunar crust. Geophys. Res. Lett. 41, 5771–5777. doi:10.1002/2014GL060240.

Beyer, R.A., Alexandrov, O., Moratto, Z.M., 2014. Aligning terrain model and laser altimeter point clouds with the Ames stereo pipeline. In: Lunar and Planetary Science Conference, p. 2902.

Fassett, C.I., et al., 2012. Lunar impact basins: Stratigraphy, sequence and ages from superposed impact crater populations measured from Lunar Orbiter Laser Altimeter (LOLA) data. J. Geophys. Res. (Planets) 117, 0. doi:10.1029/2011JE003951.

Haruyama, J., et al., 2008. Global lunar-surface mapping experiment using the Lunar Imager/Spectrometer on SELENE. Earth, Planets, Space 60, 243–255. doi:10.1186/BF03352788.

Haruyama, J. et al., 2012. Lunar global digital terrain model dataset produced from SELENE (Kaguya) terrain camera stereo observations. In: Lunar and Planetary Science Conference, p. 1200.

Haruyama, J. et al., 2014. Data products of SELENE (Kaguya) Terrain Camera for future lunar missions. In: Lunar and Planetary Science Conference, p. 1304.

Head, J.W., et al., 2010. Global distribution of large lunar craters: Implications for resurfacing and impactor populations. Science 329, 1504. doi:10.1126/science.1195050.

Huber, P.J., 1991. Robust Statistics. John Wiley & Sons, Inc., New York 320 pages, ISBN: 0471418056, 9780471418054.

Johnson, A., et al., 2010. An integrated traverse planner and analysis tool for planetary exploration. Am. Inst. Aeronaut. Astronaut. doi:10.2514/6.2010-8829, http://dx.doi.org/10.2514/6.2010-8829.

Kamalakar, J.A. et al., 2009. Laser ranging experiment aboard Chandrayaan-I: Instrumentation and preliminary results. In: Lunar and Planetary Science Conference, p. 1487.

Lagarias, J.C., et al., 1998. Convergence properties of the Nelder–Mead simplex method in low dimensions. SIAM J. Optimiz. 9, 112–147. doi:10.1137/S1052623496303470, http://dx.doi.org/10.1137/S1052623496303470.

Lemoine, F.G., et al., 2014. GRGM900C: A degree 900 lunar gravity model from GRAIL primary and extended mission data. Geophys. Res. Lett. 41, 3382–3389. doi:10.1002/2014GL060027.

Liu, J.J. ,et al., 2009. Automatic DEM generation from CE-1's CCD Stereo Camera images. In: Lunar and Planetary Science Conference, p. 2570.

Mazarico, E. et al., 2013. Improved precision orbit determination of Lunar Orbiters from the GRAIL-derived lunar gravity models. In: 23rd AAS/AIAA Space Flight Mechanics Meeting, pp. 13–274.

Mazarico, E., et al., 2014. Detection of the lunar body tide by the Lunar Orbiter Laser Altimeter. GRL 41, 2282–2288. doi:10.1002/2013GL059085.

Melosh, H., 1989. Impact Cratering: A Geologic Process. Oxford Monographs on Geology and Geophysics. Oxford University Press, London.

Murphy, T.W., et al., 2011. Laser ranging to the lost Lunokhod 1 reflector. Icarus 211, 1103–1108. doi:10.1016/j.icarus.2010.11.010.

Neumann, G., 2010. Lunar Orbiter Laser Altimeter Spherical Harmonic ASCII Data Record (LRO-L-LOLA-5-SHADR-V1.0). NASA Planetary Data System, 2010; data set released on 15 March 2010.

Neumann, G.A., et al., 1996. The lunar crust: Global structure and signature of major basins. J. Geophys. Res. 101, 16841–16864. doi:10.1029/96JE01246.

Ohtake, M., et al., 2008. Performance and scientific objectives of the SELENE (KAGUYA) Multiband Imager. Earth, Planets, Space 60, 257–264. doi:10.1186/BF03352789.

Pike, R.J., 1976. Crater dimensions from Apollo data and supplemental sources. Moon 15, 463–477. doi:10.1007/BF00562253.

Ping, J., et al., 2009. Lunar topographic model CLTM-s01 from Chang'E-1 laser altimeter. Sci. China: Phys., Mech. Astron. 52, 1105–1114. doi:10.1007/s11433-009-0144-8.

Potts, N.J., et al., 2015. Robotic traverse and sample return strategies for a lunar farside mission to the Schrödinger basin. Adv. Space Res. 55, 1241–1254. doi:10.1016/j.asr.2014.11.028.

Radhadevi, P.V., et al., 2013. An algorithm for geometric correction of full pass TMC imagery of Chandrayaan-1. Planet. Space Sci. 79, 45–51. doi:10.1016/j.pss.2013.01.012.

Scholten, F., et al., 2012. GLD100: The near-global lunar 100 m raster DTM from LROC WAC stereo image data. J. Geophys. Res. (Planets) 117, 0. doi:10.1029/2011JE003926.

Smith, D.E., et al., 1997. Topography of the Moon from the Clementine LIDAR. J. Geophys. Res. 102, 1591. doi:10.1029/96JE02940.

Smith, D.E., et al., 2010. Initial observations from the Lunar Orbiter Laser Altimeter (LOLA). Geophys. Res. Lett. 37, 18204. doi:10.1029/2010GL043751.

Smith, D.E., et al., 2010. The Lunar Orbiter Laser Altimeter investigation on the Lunar Reconnaissance Orbiter Mission. Space Sci. Rev. 150, 209–241. doi:10.1007/s11214-009-9512-y.

Wagner, R.V., et al., 2014. Locations of anthropogenic sites on the Moon. In: Lunar and Planetary Science Conference, p. 2259.

Wieczorek, M.A., 2007. Gravity and topography of the terrestrial planets. Treat. Geophys. 10, 165–206. doi:10.1016/B978-044452748-6/00156-5.

Wieczorek, M.A., Phillips, R.J., 1998. Potential anomalies on a sphere – Applications to the thickness of the lunar crust. J. Geophs. Res. 103, 1715. doi:10.1029/97JE03136.

Wieczorek, M.A., et al., 2013. The crust of the Moon as seen by GRAIL. Science 339, 671–675. doi:10.1126/science.1231530.

Williams, J.G., Boggs, D.H., Folkner, W.M., 2008. DE421 Lunar Orbit, Physical Librations, and Surface Coordinates. Jet Propulsion Lab., Calif. Inst. of Technol., Pasadena, Calif.

Williams, J.G., Boggs, D.H., Folkner, W.M., 2013. DE430 Lunar Orbit, Physical Librations, and Surface Coordinates. Jet Propulsion Lab., Calif. Inst. of Technol., Pasadena, Calif.

Zuber, M.T., et al., 2013. Gravity field of the Moon from the Gravity Recovery and Interior Laboratory (GRAIL) mission. Science 339, 668–671. doi:10.1126/science.1231507.